Recombination centers in 4H-SiC investigated by electrically detected magnetic resonance and ab initio modeling

J. Cottom,[1, a)] G. Gruber,[2, 3, a)] P. Hadley,[3] M. Koch,[4] G. Pobegen,[2] T. Aichinger,[5] and A. Shluger[1]

[1)] *University College London - Department of Physics & Astronomy, Gower Street, London, WC1E 6BT, United Kingdom*[b)]

[2)] *KAI GmbH, Europastraße 8, 9500 Villach, Austria*

[3)] *Institute of Solid State Physics - Graz University of Technology, Petersgasse 16, 8010 Graz, Austria*

[4)] *Institute of Experimental Physics - Graz University of Technology, Petersgasse 16, 8010 Graz, Austria*

[5)] *Infineon Technologies, Siemensstraße 2, 9500 Villach, Austria*

(Dated: 2 February 2016)

Electrically detected magnetic resonance (EDMR) is a powerful technique for the observation and categorization of paramagnetic defects within semiconductors. The interpretation of the recorded EDMR spectra has long proved to be challenging. Here defect spectra are identified by comparing EDMR measurements to extensive *ab initio* calculations. The defect identification is based upon the defect symmetry and the form of the hyperfine (HF) structure. A full description is given of how an accurate spectrum can be generated from the theoretical data by considering some thousand individual HF contributions out of some billion possibilities. This approach is illustrated with a defect observed in nitrogen implanted silicon carbide (SiC). Nitrogen implantation is a high energy process that gives rise to a high defect concentration. The majority of these defects are removed during the dopant activation anneal, shifting the interstitial nitrogen to the desired substitutional lattice sites, where they act as shallow donors. EDMR shows that a deep-level defect persists after the dopant activation anneal. This defect is characterized as having a $g_{c\|B} = 2.0054\,(4)$ and $g_{c\perp B} = 2.0006\,(4)$, with pronounced hyperfine shoulder peaks with a 13 G peak to peak separation. The nitrogen at a carbon site next to a silicon vacancy ($\mathrm{N_C V_{Si}}$) center is identified as the persistent deep-level defect responsible for the observed EDMR signal and the associated dopant deactivation.

---

[a] J. Cottom and G. Gruber contributed equally to this work.

[b] j.cottom.12@ucl.ac.uk

I. INTRODUCTION

Understanding and identifying defects in semiconductor devices is key in achieving improved device performance, which has long proved challenging. One material where this is particularly important is silicon carbide (SiC) because of the suitability of this semiconductor as a base material for high power and high temperature devices[1,2]. The most relevant polytype from a device perspective is 4H-SiC, which has a band gap of 3.26 eV at room temperature. In *n*-type 4H-SiC, nitrogen has emerged as the most feasible shallow donor impurity due to its low mass and its low ionization energy[3]. In order to form *n*-doped regions, nitrogen is typically incorporated by ion implantation and substitutes preferentially for carbon rather than for silicon[4–6]. For the N substitutional donor (N_C) there is a slight difference in ionization energy dependent on whether it sits at the quasi-hexagonal site (60 meV) or in the quasi-cubic site (120 meV)[7,8]. In device regions where high conductivity is desired, particularly high nitrogen doping concentrations ($\approx 10^{19}\,\mathrm{cm}^{-3}$) are required.

As the nitrogen concentration can exceed the donor concentration, it has been suggested that not all implanted nitrogen impurities occupy regular substitutional lattice sites where they can act as shallow donors[9]. Nitrogen may form silicon nitride clusters or complexes with intrinsic crystal defects such as vacancies or antisites, thereby becoming lower in energy and electrically inactive. Besides deactivating dopants, impurity defect complexes may also introduce deep levels in the SiC band gap, which can act as recombination centers and limit the performance of SiC devices. Theoretical and experimental investigations have shown that nitrogen is able to interact with silicon vacancies (V_{Si}), carbon vacancies (V_C), divacancies ($V_{Si}V_C$) and vacancy clusters to form either N_CV_{Si} or $N_{Si}V_C$[5]. The fully passivated $(N_C)_4\,V_{Si}$ defect, which is an electrically passive defect, has also been suggested as a candidate for dopant deactivation[5].

In numerous previous electron paramagnetic resonance (EPR) studies performed on N-doped SiC the spectra were dominated by the shallow N_C dopants[10–13]. Some studies reported on an additional smaller signal of a defect with smaller concentration, called the N_x center[11–14]. This defect has been assigned to the shallow N_C dopants as well[11,13,14]. There is only one study applying conventional EPR in order to measure a nitrogen-complexed defect[15]. This identification was possible due to a large zero-field splitting resulting from the spin S=1 of the defect which was identified as the negatively charged NV-center ($N_CV_{Si}^{-1}$).

However, the studied sample was not a fully processed device but rather a sample specifically treated for maximizing the concentration of NV-centers. It is therefore not clear from that study, whether the N_CV_{Si} defect is also present in fully operational devices, where high temperature anneals are a standard process to reduce the number of unwanted defects. In a recent study by Aichinger *et al.* the spectra of deep levels caused by N implantation were unambiguously measured in fully processed *pn*-junctions using the spin dependent recombination (SDR) technique[16]. A well resolved spectrum was measured in N-implanted SiC devices, which was not observed in epitaxially grown devices. A very similar defect was also observed in another SDR study on *pn*-junctions in bipolar junction transistors[17]. Small scale theoretical modeling appeared to assign the observed spectrum to the substitutional N next to a C antisite (N_CC_{Si}) although this assignment is in question[18]. The basis of the concern arises from discrepancies in the magnitudes of the hyperfine (HF) peaks and that the symmetry of the experimentally observed defect seems at odds with the assignment of N_CC_{Si}.

While SDR as opposed to EPR does not give any reliable information on the concentration of the defects, it is the only method to study the structure of deep defects in these fully working devices. The benefit of using this technique comes from the fact that the shallow defects are not detected. Therefore, the response the deep defects is not overshadowed by the signal of the high concentration of the dopants. In the present study we compare spectra from N implanted *pn*-junctions obtained by SDR with extensive simulations and detailed probabilistic treatment of the calculated hyperfine parameters in order to identify the structure of the dominant defect. The results demonstrate that the nitrogen at a carbon site next to a silicon vacancy N_CV_{Si} center is the persistent deep-level defect responsible for the observed SDR signal and the associated dopant deactivation.

II. METHODOLOGY

A. Experimental

Electrically detected magnetic resonance (EDMR) makes it possible to investigate performance limiting defects directly on fully processed devices, *e.g.* a *pn*-junction. Here we use SDR, a subset of EDMR where a recombination current is used to measure the transitions between the Zeeman levels of paramagnetic recombination centers in the studied sample[17,19,20]. The technique is most sensitive to paramagnetic defects close to the middle of the band gap, as they are the most efficient recombination centers[20–23]. Fig. 1 shows a schematic of how SDR is performed. A *pn*-junction is forward biased so that electrons and holes are injected into the depletion region of the junction. The total current I through the *pn*-junction is a sum of a diffusion current I_{diff} and a recombination current I_{rec}. The recombination component of the current depends on the density of recombination centers in the depletion region of the junction which can capture electrons and holes and allows them to recombine. The device under test is put in a microwave cavity where a quasi-static external magnetic field B is applied. As this magnetic field interacts with the electron spins the recombination rates are lowered[24]. Additionally, a microwave field is applied of which the magnetic component B_{mw} interacts with the spins. When resonance occurs, the recombination rates are enhanced and a change in the current (ΔI) can be observed[19,24]. The resonance condition is

$$h\nu = g\mu_{\text{B}}\left(B_{\text{res}} + \sum_{k=1}^{n} a_k m_k\right) \tag{1}$$

where h is Planck's constant, ν is the microwave photon frequency, g is the Landé-factor, μ_{B} is the Bohr magneton, B_{res} is the resonant applied magnetic flux density, a_k is the HF splitting constant at atomic site k, m_k is the magnetic nuclear spin quantum number at atomic site k, and k sums over the atoms that make up the defect[25].

One way to identify a defect is to analyze the g-factor which is influenced by the local environment of a specific defect. Even when a strong resonance peak is observed in an experiment, it is not always obvious what the microscopic structure of the defect is. While g can be calculated for a candidate defect, a precise calculation is very challenging[26]. However, the observed angular dependence of g must match the symmetry of the defect.

Another way to identify a defect is to examine the additional structure caused by the HF interaction. The sum over HF constants in (1) shifts the field where the resonance occurs and adds satellite peaks to the spectrum. Every atom with a non-zero nuclear spin on a site where the electron density is non-negligible adds a contribution to the HF structure. As the unpaired electron wave function can extend over the nearest neighbor (1NN), the second nearest neighbor (2NN) and even the third nearest neighbor (3NN) shells, there may be many contributions to the sum. Paired with the fact that SDR spectra are often broadened, this can make the interpretation more difficult[16,18].

Theoretical modeling combined with accurate probabilistic consideration of the calculated HF interactions can be used to identify the defect responsible for the observed SDR spectra, as discussed below.

FIG. 1. Schematic of an SDR measurement. The sample is in a microwave cavity with a microwave field of frequency ν and a magnetic field component B_{mw} which is marked by dotted arrows. The externally applied magnetic field B is directed into the plane. The device is forward biased at V_{f} and the current I is measured.

1. Experimental parameters

We studied a 4H-SiC *pn*-junction which was formed by heavy N implantation (doping of $5 \times 10^{17}\,\mathrm{cm}^{-3}$) and an Al implantation of a similar dose. The sample received a standard dopant activation anneal at 1800 °C. The measurements were recorded similarly to those of Aichinger *et al.*[16]. To measure SDR, the sample was forward biased at $V_{\mathrm{f}} = 2.35\,\mathrm{V}$, which is in the regime where recombination is high and a good signal-to-noise ratio can be obtained. The sample was measured at room temperature with an X-band EPR spectrometer at a microwave frequency of $\nu \approx 9.402\,\mathrm{GHz}$ and a microwave power of $\approx 50\,\mathrm{mW}$. The magnetic field was calibrated using a 2,2-diphenyl-1-picrylhydrazyl standard and a Drusch nuclear magnetic resonance magnetometer. The current was measured with a Stanford Research SR570 current amplifier and a Stanford Research SR830 lock-in-amplifier. For the lock-in-amplification a magnetic field modulation of 0.5 G was applied in order to avoid any line broadening by over-modulation and to obtain the best resolution of the HF side peaks. The modulation frequency was $\approx 900\,\mathrm{Hz}$. Due to the use of lock-in amplification, all spectra were recorded as $\mathrm{d}I/\mathrm{d}B$ vs. B. Multiple scans were averaged to improve the signal-to-noise ratio.

B. Theoretical simulations

Density functional theory calculations were performed using the CP2K code; the functionals selected for the calculations were PBE and HSE06[27–29]. These functionals were utilized with the DZVP-MOLOPT-SR-GTH and the TZVP-MOLOPT-GTH basis sets[30]. This led to the selection of a $5\times4\times2$ orthorhombic 4H-SiC supercell (480 atoms - 15 Å × 16 Å × 20 Å). This formed the basis for all of the calculations allowing for the defect relaxation to be contained within the simulation supercell. All parameters were converged to 0.01 meV per formula unit. The cell parameters of the bulk 4H-SiC and the defect geometries were relaxed using the HSE06 functional as stated above. It was found that by employing a pre-optimization with the PBE functional reduced the required the number of optimization steps required to converge the subsequent HSE06 structure. This offered a substantial saving in computational time and as such was employed on all of the defect calculations. This approach gives the HSE06 defect geometry and electronic structure which has been show to perform very well for the 4H-SiC system and defects contained within[31].

The HF parameters were calculated using the Gaussian augmented-plane wave (GAPW) approximation in the CP2K code[27]. The basis-sets selected for geometry optimization (above) are not appropriate for the calculation of hyperfine parameters, as an explicit description of the core electrons and hence an all electron basis set is required. To ensure the best description of the core electrons, extensive calibration and testing of several basis-sets was conducted using a variety of test systems. These included both simple molecular and solid state radicals with unambiguously identified HF parameters. The best accuracy was obtained from the pcj family of basis-sets[32] with an error of ±6 G in the pcj-0 case, ±3 G for pcj-1 and ±1 G for pcj-2 and pcj-3. As a result of these calibration tests, the pcj-1 basis set was selected as giving the best balance of accuracy to computational time.

1. *Defect Calculation*

The above parameters and supercells were used for all defect calculations. Initially the neutral charge states were calculated and from the number of occupied and unoccupied gap states, the accessible charge states for a given defect were inferred and calculated. The defect formation energy E_f was calculated using the standard formalism of Northrup and Zhang[33]. This neglects the temperature dependent portion of the free energy of formation, (Ω_f=E_f-TS) which includes phonon effects that are challenging to calculate. While E_f dominates at low temperatures, the entropy term (S) can have a marked effect on Ω_f at elevated temperatures. Explicit consideration of this is beyond the scope of this work and the E_f is assumed to approximate Ω_f as

$$E_\mathrm{f} = E_\mathrm{d}(q) + \sum_s n_s\mu_s + q(E_\mathrm{V} + \mu_\mathrm{e}) - E_\mathrm{bulk}, \tag{2}$$

where E_f for each charge state (q) is measured relative to the valence band maximum E_V, μ_e is the Fermi energy, μ_s is the chemical potential of species s, and E_d is the total energy of the defective supercell, while E_bulk is the total energy of the defect free bulk. It is important to note that the lowest energy charge state for a given μ_e assumes that the system has reached thermodynamic equilibrium, which may not always be the case. With this in mind, formation energies give useful information about the relative concentrations for a given series of defects. The chemical potentials are treated in accordance with the method outlined by Torpo *et al.*[34] with 1/2 of N_2 molecule total energy used for the μ_N. Finite size charge corrections are applied according to the scheme of Lany and Zunger with consideration of the anisotropic nature of the supercell using the methodology of Murphy and Dines[35,36].

C. Probabilistic treatment of HF parameters

In order to simulate a spectrum one needs to find the positions of the resulting HF side peaks from the calculated data to be discussed in section V. Rewriting (1) reveals the resonance field B_res for a given configuration of n atoms as

$$B_\mathrm{res} = B_0 - \sum_{k=1}^{n} a_k m_k. \tag{3}$$

The term $B_0 = h\nu/(g\mu_\mathrm{B})$ is simply the resonance field without HF interactions and marks the center of the spectrum. For a given defect many different configurations of the m_k values of the n atoms are possible, each resulting in a different HF interaction term in (3). Only defects containing N, Si and C are to be considered, see IV. At a nitrogen site, m can take on the values -1, 0, or 1 assuming that 100% of the nitrogen is ^{14}N which has a nuclear spin of 1. At a carbon site, $m = 0$ for a ^{12}C isotope and $m = \pm 1/2$ for a ^{13}C isotope. At a silicon site, $m = 0$ for the ^{28}Si and ^{30}Si isotopes and $m = \pm 1/2$ for the ^{29}Si isotope. Therefore, every atomic site has three possible spin states with a respective probability. As the isotopes are randomly placed around the defect, for n atoms there are 3^n possibilities to consider. Each of these will shift the center of the Lorentzian peak and the experimentally observed result will be a sum of all of these resonance peaks. In an experiment, the weighted sum of all lines due to the individual configurations is measured. The intensity P of each individual line is given by the product of the probability $p(\mathrm{atom}_k, m_k)$ for each atom at site k to have a certain spin state

$$P = \prod_{k=1}^{n} p(\mathrm{atom}_k, m_k) \tag{4}$$

with $p(\mathrm{N}, 0) = p(\mathrm{N}, \pm 1) = 1/3$, $p(\mathrm{C}, 0) = 0.989$, $p(\mathrm{C}, \pm 1/2) = 0.0055$, and $p(\mathrm{Si}, 0) = 0.953$, $p(\mathrm{Si}, \pm 1/2) = 0.0233$. The resulting line at the position B_{res} can be represented by a Lorentzian lineshape $L \propto P/(\Gamma^2 + B - B_{\mathrm{res}})^2$ with Γ being a parameter linked to the line width via $W_{\mathrm{pp}} = 2/\sqrt{3}\Gamma$. The experiments are performed with a lock-in amplifier and the measured signal is the sum of the derivatives of the Lorentzians. The resulting contribution of one set of n atoms with their respective spin states m_k can be represented by a derivative Lorentzian line given by

$$L'(B; B_{\mathrm{res}}; \Gamma) = \frac{-P\,(B - B_{\mathrm{res}})}{\left[\Gamma^2 + (B - B_{\mathrm{res}})^2\right]^2}. \tag{5}$$

In order to simulate a complete spectrum it is necessary to sum over all 3^n permutations of the m_k of the n atoms. The equation that describes the full spectrum can be written as

$$L'_{\mathrm{total}} = \sum_{i_1=1}^{3} \sum_{i_2=1}^{3} \ldots \sum_{i_n=1}^{3} \left(-\prod_{k=1}^{n} p(\mathrm{atom}_k, m_k) \frac{B - B_0 + \sum_{k=1}^{n} a_k m_{k,i_k}}{\left[\Gamma^2 + \left(B - B_0 + \sum_{k=1}^{n} a_k m_{k,i_k}\right)^2\right]^2} \right). \tag{6}$$

The defects considered contain up to about 30 individual atoms interacting with the unpaired electron. Simulating the full spectrum including all lines therefore requires enormous computational resources and is not practical. Fortunately, many of the configurations are improbable and can be neglected. For instance, it is exceedingly unlikely that all of the carbon atoms in the neighborhood of the defect are ^{13}C isotopes. By setting a minimum probability P_{min} to be considered one can dramatically reduce the number of lines that are actually calculated. Subsequently we consider only lines with a higher abundance than $P_{\mathrm{min}} = 10^{-7}$ when generating the simulated spectra. In order to prevent memory problems, the 3^n atoms are split into smaller subsets where all combinations of nuclei resulting in a smaller probability than P_{min} are filtered out. In a second step, the remaining sets are combined and again a filtering step is applied. In the end, the total of 3^n lines to be plotted are reduced by many orders while still $> 99\%$ of the total spectrum is simulated. The advantage of this method is that every splitting constant of every atom can be considered individually rather than using an average value. Also very small contributions are considered even though they do not result in resolved features. However, they can add broadening to the line and influence the resulting line shape which otherwise may not be well represented.

III. EXPERIMENTAL RESULTS

The recorded spectra with the crystalline c-axis oriented parallel to the magnetic field B ($c \parallel B$) and with c oriented perpendicular to B ($c \perp B$) are shown in Fig. 2. The former corresponds to B applied in the [0001] direction and the latter to B in the $[1\bar{1}00]$ direction, respectively. The measured g-values are $g_{c\parallel B} = 2.0054\,(4)$ and $g_{c\perp B} = 2.0006\,(4)$. The spectra are rotationally symmetric about the crystalline c-axis with some small deviations (likely due to the 4° off-axis growth) within experimental error. The spectrum with the magnetic field applied in the $[11\bar{2}0]$ direction is equivalent to $[1\bar{1}00]$ and is therefore not shown. The spectrum with $c \parallel B$ is slightly sharper, which can be explained by the hexagonal crystal structure and more defect atoms being equivalent in this direction. There is some small anisotropy in the HF interaction as the main side features in the $c \parallel B$ direction are split into two sets of lines in the $c \perp B$ direction. It is likely that this is due to equivalent sites in the former direction being inequivalent in the latter.

For simplicity, all of the following considerations focus on the $c \parallel B$ spectrum. The spectrum contains a strong center line with a peak-to-peak linewidth of $W_{\mathrm{pp}} \approx 3.8\,\mathrm{G}$ and several HF side peaks. The most pronounced peaks are at approximately $\pm 6.5\,\mathrm{G}$ left and right of the center line. Due to their high relative intensity, the lines are likely either to be due to the HF interaction of one N atom, as suggested by Aichinger *et al.*[16], or due to multiple Si atoms, as they can in sum have a significant abundance as well. A second pair of HF lines with much smaller relative intensity is found at approximately $\pm 21\,\mathrm{G}$ and is likely due to a few C atoms. No more lines with a larger splitting than the ones mentioned were observed in the region $\pm 600\,\mathrm{G}$ away from the center line. In the following sections we use theoretical modeling of the defect structures and compare them to the SDR spectra in order to identify the responsible defect.

FIG. 2. SDR spectra of N-implanted pn-junctions recorded with $c \parallel B$ and $c \perp$ B.

IV. THEORETICAL RESULTS

In this study we are only interested in defects present in N-implanted devices[16]. Therefore the initial calculations are concerned with defects containing N either at a substitutional site or as a defect complex, such as $N_C C_{Si}$, $N_C V_{Si}$, $N_{Si} V_C$, $N_C N_{Si}$, N_{Si}, N_C, and N_i. These defects in all of the accessible charge states form the defect 'long list' considered as potential candidates for a center responsible for the SDR signal described above. They were then assessed further on the basis of accessible paramagnetic gap states and formation energy, which leaves the defect 'short list' containing the lowest energy accessible paramagnetic states for each distinct defect configuration. These states would be visible to SDR and hence should be investigated further.

In addition, while the substitutional and interstitial defects have been included for completeness, they have been subject to extensive characterization[5,6,14,37–41]. This leaves the following defects $N_C C_{Si}^0$, $N_C V_{Si}^{0,-1,-2}$, and $N_{Si} V_C^{+2}$.

A. Defect short list ($N_C V_{Si}$, $N_{Si} V_C$ and $N_C C_{Si}$)

Nitrogen is envisaged to interact with either a pre-existing divacancy to form an NV center, or to substitute for an atom adjacent to a vacancy. These defects have been considered previously[5,6] and are easily within the energetic span provided by the implantation process and subsequent dopant activation anneal. The $N_C V_{Si}$ has additionally gained a degree of recent attention from a quantum computing perspective. It has been proposed that the $N_C V_{Si}^{-1}$ defect[15,42,43], among some other point defects in SiC[42–50], has the potential to act as a qubit. These properties have been extensively cataloged and compared to the diamond NV center, an existing qubit system[15,42,43,45,46]. Fig. 3 shows the formation energy of the defects on the short list. The defect configurations are shown in Fig. 4, Fig. 5, and Fig. 6 for the $N_C V_{Si}$, $N_{Si} V_C$, and $N_C C_{Si}$ defects, respectively. The $N_C V_{Si}$, and $N_{Si} V_C$ are clearly related, whereas the $N_C C_{Si}$ is very different, with a carbon antisite precursor being required.

1. $N_C V_{Si}$

The $N_C V_{Si}$ (Fig. 4) is accessible in the 0, -1, and -2 charge states (Fig. 3). The neutral charge state has a doublet ground state with a quartet state being only 0.10 eV higher in

FIG. 3. Combined formation energy plot. The $N_{Si}V_C$ is represented by the solid (red) line, the N_CV_{Si} is the dashed (blue) line, and the N_CC_{Si} is shown by the double dashed (green) line. The bold lines indicates the lowest energy charge states for each conformation as a function of Fermi level position. The $N_{Si}V_C$ and the N_CV_{Si} are considered together as they represent rearrangements of the same defect. In each case it is the lowest energy conformation, hh, that is plotted. An energetic span of 0.05 eV covers all conformations. This is approximated by the linewidth.

energy. The Si-N bond length is 1.79 Å and the Si-C* (C* - 3-coordinate carbon) bond length is 1.75 Å. This similarity leads to little strain induced in the structure from the introduction of N at the C site. The defect has either C_{1h} (low spin) or C_{3v} (high spin) symmetry with three sp^3 hybridized carbon dangling bonds. The defect-induced lattice deformation propagates in the same manner as in the V_{Si} in the directions defined by the 3 carbon dangling bonds, with the bulk bond length being recovered within ≈ 7 Å. As there is little correlation between the three carbon dangling bonds, the doublet and quartet states are separated by only 0.10 eV.

As the Fermi energy approaches the conduction band of SiC, gradually higher negative charge states become accessible, the 0/-1 transition is at ≈ 1.3 eV, -1/-2 at 1.8 eV and -2/-3 at 2.9 eV.

The even charge states are paramagnetic in the low spin state (doublet), the -1 charge state has a high spin (triplet) ground state. The result is that the N_CV_{Si} defect is paramagnetic and hence visible to SDR at most Fermi energy positions within the SiC band gap. However, for the -1 charge state a large zero-field splitting due to the electron-electron coupling has been reported[15]. The respective lines were not observed in the SDR measurements, which rules out this charge state. In the neutral charge state it has a formation energy of 4.82 eV compared to the defect free bulk.

2. $N_{Si}V_C$

The $N_{Si}V_C$ (Fig. 5) defect appears markedly different with the N-C bond being significantly shorter than the N-Si bond. Incorporating the N at the silicon site results in a more distorted structure. The N is forced back into the plane of the C atoms leading to a more planar arrangement than in the N_CV_{Si}, as is clearly seen in Fig. 4. This distortion

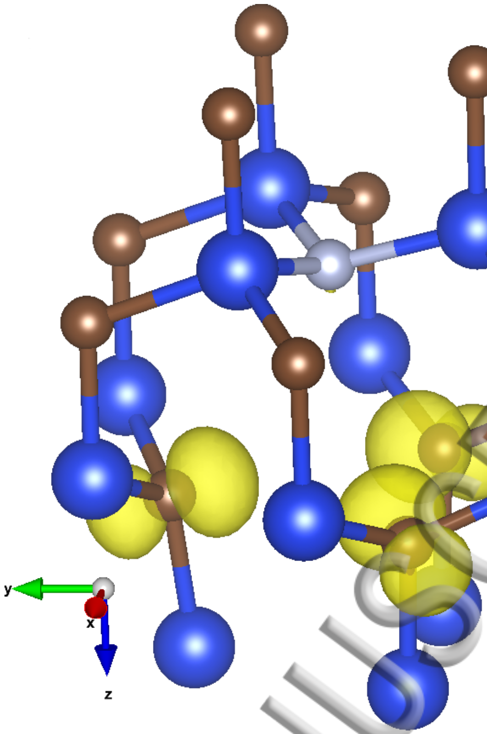

FIG. 4. The spin density plot for the $N_CV_{Si}^0$, illustrating the C_{3v} symmetry of the defect, with the principle symmetry axis aligned along the crystal c-axis. The spin density is concentrated on the 3 C dangling bonds (sp^3 hybridized). C atoms are brown, Si are blue and N is white.

of the N-C bond leads to a repulsive interaction with the nitrogen lone pair resulting in non-bonding N states within the SiC band gap. This behavior contrasts with the V_C, where the 3-coordinated Si atoms are able to pair forming two long range Si-Si interactions. This is only possible for two of the 3-coordinated Si leaving one lone Si dangling bond in the neutral charge state. In the +2 charge state the spin density is centered almost entirely ($> 99\%$) on the N. The +1 charge state sees the ionization of the Si dangling bond. The $N_{Si}V_C$ is only favored in the heavily p-type regime close to the valence band (VB), with only the +2 charge state being accessible for 0.4 eV next to the VB. The neutral defect has a formation energy significantly higher than that of the N_CV_{Si} at 8.02 eV compared to the bulk. This defect is only accessible in a Fermi energy range next to the VB and would not be expected to be observable with SDR. In addition, when considering the symmetry of the defect over all sites (isotropic) it does not provide the required anisotropy. Therefore it can be discarded as a potential candidate.

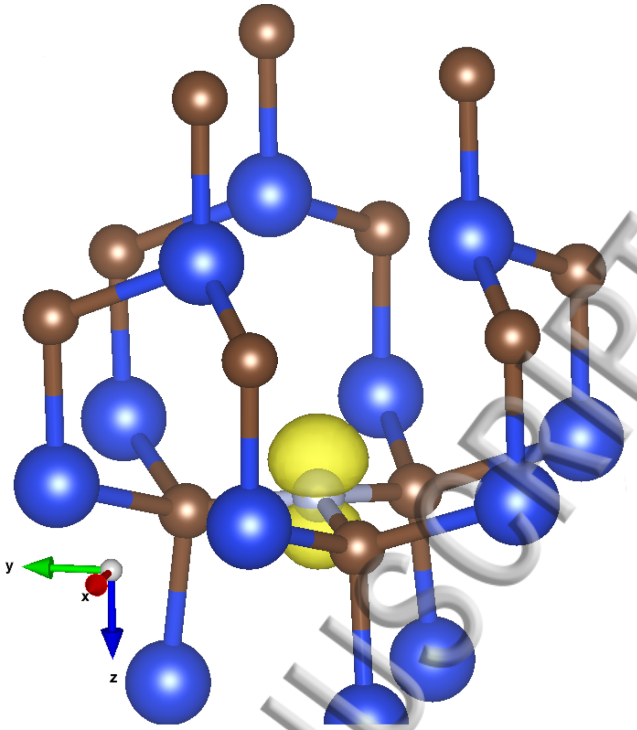

FIG. 5. The spin density plot for the $N_{Si}V_C^{+2}$, illustrating the planar arrangement of the radical centered on nitrogen p-states, resulting from ionization of the nitrogen lone pair. C atoms are brown, Si are blue and N is white.

3. $N_C C_{Si}$

For completeness $N_C C_{Si}$ is considered representing the rearrangement of the silicon vacancy to form the vacancy antisite pair. It is clear that the $N_C C_{Si}$ has the +1 charge state favored for the first half of the SiC band gap with a charge transition level at 1.6 eV when the neutral charge state is favored (Fig. 3). As with the previous defects where N sits at the C site, the N-C bond length is 1.78 Å and the N is accommodated with little distortion to the lattice. In the case of the C at the silicon site, the C-C bond length is substantially shorter at 1.57 Å leading to an inward relaxation of the neighboring C atoms (Fig. 6). This forms a near planar C radical with respect to the neighboring C. In the neutral defect state. the unpaired electron sits on the 3 coordinate C within a p-type orbital. In the +1 charge state the unpaired electron is lost forming a planar carbocation, the +1 charge state is not paramagnetic and invisible to SDR.

Before considering the hyperfine parameters of shortlisted defects, we note that the sym-

AIP Publishing

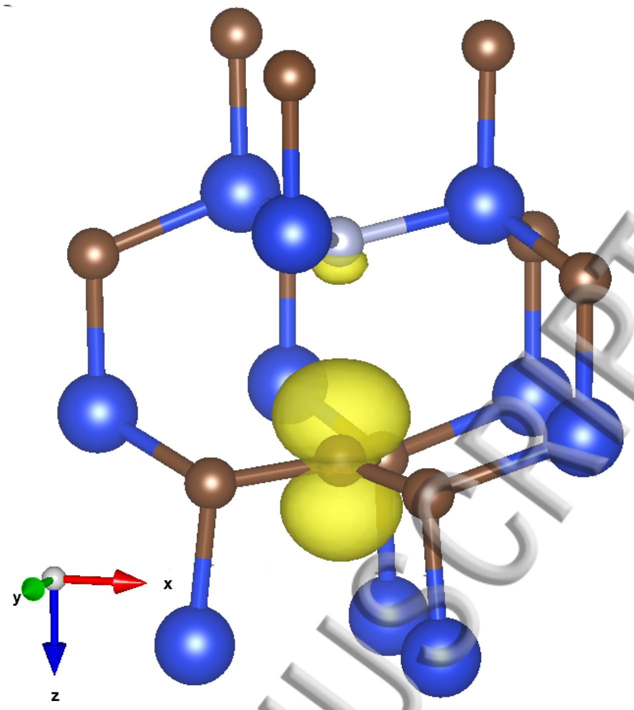

FIG. 6. The spin density plot for the $N_CC^0_{Si}$, illustrating the highly directional planar carbon p-centred radical. When all configurations are considered the defect would appear isotropic. The spin density is centered on the 3-coordinate C_{Si}. C atoms are brown, Si are blue and N is white.

metries of the defects discussed above seems to rule out both the $N_CC^0_{Si}$ and $N_{Si}V_C^{+2}$. The experimentally observed defect shows a pronounced rotational symmetry about the crystal c-axis along with an anisotropy with respect to the crystal c-axis. Both the $N_CC^0_{Si}$ and the $N_{Si}V_C$ defects can be approximated by the $C_{\infty v}$ point group, but when considered in every possible orientation this gives a defect of T_d symmetry which lacks the required anisotropy with respect to the c-direction.

V. COMPARISON OF EXPERIMENT AND THEORY

The HF parameters of the most reasonable defects complexes with their paramagnetic deep level charge states are shown in table I. This table only contains averaged values for the equivalent atoms that have significant HF splitting constants. However, they can be used to create an accurately simulated spectrum according to (6) in order to compare theory to experiment. Fig. 7 shows the simulated spectra compared to the experimental spectrum.

It is quite obvious that the N_CV_{Si} defect, especially in the neutral charge state, is a

FIG. 7. Experimental and simulated spectra of the most reasonable candidate defects. The simulation has been performed based on the data in table I. The spectra are scaled to the same peak-to-peak height and vertically shifted for better comparison.

much better candidate than the N_CC_{Si}. The N_CC_{Si} center does not even closely match the experimental spectrum. Although this simulation was performed with averaged a_k values including the errors outlined above, this defect has to be ruled out as reasonable candidate defect, leaving the N_CV_{Si} in its different charge states.

The $N_CV_{Si}^0$ shows the best agreement between theory and experiment as it is the only one with pronounced Si side shoulders. For this reason, a more detailed theoretical treatment of this charge state has been performed. An important point that has been left out so far is the fact that the N atom can sit in four different sites with respect to the V_{Si}. Additionally, the V_{Si} can sit in a quasi-cubic (k) or quasi-hexagonal (h) site. Therefore, a total of four different configurations, two of which (hk and kh) are triply degenerate (kk, $kh_{1,2,3}$, hh, $hk_{1,2,3}$) are possible, each with a slightly different formation energy and electronic structure. In order to improve the simulation of the resulting spectrum each of the four defect configurations were calculated. The resulting a_k values for every atom of every configuration were used explicitly in the simulations of the spectra, rather than their average or single configuration values. All this data can be found in the supplementary material[51]. The resulting spectra have been simulated and added together. Their individual contributions were weighted with their respective Boltzmann factors corresponding to their formation energies. The resulting

TABLE I. Calculated HF splitting constants a_k for the most reasonable candidate defects in their different paramagnetic charge states. The values were calculated using the pcj-1 basis-set, with the HSE06 functional. a_{C1} refers to the equivalent atoms 1NN C shell, a_{Si2} to the 2NN Si shell, and a_{C3} to the 3NN C shell. The values are averaged for all atoms in the same shell.

Defect	a_N (G)	a_{C1} (G)	a_{Si2} (G)	a_{C3} (G)
$N_CV_{Si}^0$	0.8	39.9	10.7	6.7
$N_CV_{Si}^{-1}$	0.7	45.6	8.9	4.6
$N_CV_{Si}^{-2}$	0.8	46.7	9.2	6.1
$N_CC_{Si}^0$	11.2	39.9	10.7	6.7

FIG. 8. Experimental and simulated spectra generated from the weighted average of the individual defect sites of $N_C V_{Si}^0$. The data used for the simulation can be found in the supplemental material.[51] The spectra are scaled to the same peak-to-peak height.

complete spectrum is compared to the experimental spectrum in Fig. 8.

The ±21 G lines are very well matched by the three 1NN C atoms while their a_k values are marginally underestimated. The ±13 G lines are well represented by the 2NN Si atoms, especially in terms of their relative intensity. However, the a_k values fall ≈ 2.5 G short. The calibration tests illustrated that the pcj-1 basis set used to calculate the a_k value has an error of ±3 G.

In the case of the calibration calculations it was clear that an improved description of the HF parameters could be obtained with the pcj-2/3 basis-sets. In order to demonstrate the basis-set effect, which is observed in the calibration set, the $N_C V_{Si}^0$ was calculated with the pcj-3 basis-set. This in effect shrinks the discrepancy between the simulated and experimental measurements. As these calculations are very time intensive they could not be performed on all sites. Only the ground state (hh) site of the $N_C V_{Si}^0$ was calculated for comparison and the difference between pcj-1 and pcj-3 was gauged. This gives confidence that the trends suggested by the calibration set are observed, and falls well within the defined error for a given basis-set. The result is a defect with identical symmetry but with the 1NN C and 2NN Si HF splittings increased by ≈ 2.5G. Adding this shift to the a_k of all sites results in the improved simulated spectrum shown in Fig. 9 which demonstrates an excellent match between theory and experiment.

FIG. 9. Experimental and improved simulated spectra generated from the weighted average of the four individual defects sites of $N_C V_{Si}^0$. For improvement 2.5 G was added to the 1NN C and 2NN Si atoms, as suggested by the simulation using the pcj-3 basis set. The data used for the simulation can be found in the supplemental material.[51] The spectra are scaled to the same peak-to-peak height.

In a very recent study of N-implanted SiC, the $N_C V_{Si}^{-1}$ defect was identified using EPR measurements and theoretical modeling[15]. In agreement with this study we show that this defect has smaller Si HF splittings than the $N_C V_{Si}^0$ and is therefore unlikely the defect observed with SDR in this work. The large zero-field splitting observed in ref.[15] was not observed in our experiments. However, we emphasize at this point that SDR is only sensitive to the most efficient recombination center, which in our case proves to be the $N_CV_{Si}^0$ center.

VI. CONCLUSIONS

We combined SDR measurements with extensive DFT calculations to identify the best candidate of an unknown defect in a 4H-SiC *pn*-junction which was formed by heavy N implantation (doping of $5 \times 10^{17}\,\mathrm{cm}^{-3}$) and an Al implantation of a similar dose. SDR measurements were used to identify a 'fingerprint' of a defect, guiding DFT calculations of a proposed long list of defects, allowing for the selection to be narrowed down on the basis of accessible paramagnetic states, formation energy, symmetry, and hyperfine parameters.

Starting from a list of nitrogen-containing defects in SiC, N_CC_{Si}, N_CV_{Si}, $N_{Si}V_C$, N_{Si}, N_C, and N_i; it was possible to identify N_CV_{Si} as the dominant defect measured by SDR in N-implanted SiC. This defect comes in four configurations which all can exist in 3 charge states. The electron densities of the unpaired electron for these 12 cases were calculated and further the hyperfine coupling constants were determined. This made it possible to compute the hyperfine structure of the defects. While billions of lines contribute to the hyperfine structure, it was possible to sort out the few thousand lines that make the most important contribution by considering their probabilities. The observed anisotropy of the SDR spectrum describes a defect which is rotationally symmetric around the crystal *c*-axis and anisotropic with respect to the *c*-direction. This is reproduced in the C_{3v} symmetry of the calculated N_CV_{Si} defect. Therefore we conclude that the $N_CV_{Si}^0$ center is the most plausible candidate for the defect responsible for the observed SDR spectrum.

Although the N_CV_{Si} is identified as one of the deep-level defects responsible for dopant deactivation, this does not exclude the existence of other diamagnetic defects that may also be responsible for dopant deactivation.

VII. ACKNOWLEDGEMENTS

This work was jointly funded by the Austrian Research Promotion Agency (FFG, Project No. 846579) and the Carinthian Economic Promotion Agency Fund (KWF, contract KWF-1521/26876/38867). The computational work was funded via membership of the UK's HEC

Materials Chemistry Consortium, which is funded by EPSRC (EP/L000202), this work used the ARCHER UK National Supercomputing Service (http://www.archer.ac.uk). JC is funded by the Engineering and Physical Sciences Research Council, grant no EP/G036675/1 for financial support under their Centres for Doctoral Training scheme and Infineon Technologies AG. JC and AS would like to thank P. Deák and M. Bockstedte for valuable comments and discussions.

REFERENCES

[1] W. J. Choyke, H. Matsunami, and G. Pensl, *Silicon Carbide: Recent Major Advances* (Springer Science & Business Media, 2004).

[2] P. Friedrichs, T. Kimoto, L. Ley, and G. Pensl, *Silicon Carbide: Volume 1* (John Wiley & Sons, 2011).

[3] S. Seshadri, G. W. Eldridge, and A. K. Agarwal, Applied Physics Letters **72**, 2026 (1998).

[4] K. Szász, X. T. Trinh, N. T. Son, E. Janzén, and A. Gali, Journal of Applied Physics **115**, 073705 (2014).

[5] U. Gerstmann, E. Rauls, T. Frauenheim, and H. Overhof, Physical Review B **67**, 1 (2003).

[6] G. Pensl, F. Schmid, S. A. Reshanov, H. B. Weber, M. Bockstedte, A. Mattausch, O. Pankratov, T. Ohshima, and H. Itoh, Materials Science Forum **556-557**, 307 (2007).

[7] I. G. Ivanov, B. Magnusson, and E. Janzén, Physical Review B **67**, 165212 (2003).

[8] M. A. Capano, J. A. Cooper Jr., M. R. Melloch, A. Saxler, and W. C. Mitchel, Journal of Applied Physics **87**, 8773 (2000).

[9] G. Pensl, T. Frank, M. Krieger, M. Laube, S. Reshanov, F. Schmid, and M. Weidner, Physica B **340-342**, 121 (2003).

[10] S. Greulich-Weber, Physica Status Solidi A: Applications and Materials Science **162**, 95 (1997).

[11] M. E. Zvanut and J. van Tol, Physica B **401-402**, 73 (2007).

[12] E. N. Kalabukhova, S. N. Lukin, D. V. Savchenko, W. C. Mitchel, S. Greulich-Weber, U. Gerstmann, A. Poeppl, J. Hoentsch, E. Rauls, Y. Rozentzveig, E. N. Mokhov, M. Syvaejaerrvi, and R. Yakimova, Materials Science Forum **556-557**, 355 (2007).

[13] D. V. Savchenko, A. Poeppl, E. N. Kalabukhova, S. Greulich-Weber, E. Rauls, W. G. Schmid, and U. Gerstmann, Materials Science Forum **615-617**, 343 (2009).

AIP Publishing

This manuscript was accepted by J. Appl. Phys. Click here to see the version of record.

[14] U. Gerstmann, E. Rauls, S. Greulich-Weber, E. N. Kalabukhova, D. V. Savchenko, A. Poeppl, and F. Mauri, Materials Science Forum **556-557**, 391 (2007).

[15] H. J. V. Bardeleben, J. L. Cantin, S. Hamon, K. Khazen, U. Gerstmann, and E. Rauls, Physical Review B **92**, 064104 (2015).

[16] T. Aichinger, P. M. Lenahan, B. R. Tuttle, and D. Peters, Applied Physics Letters **100**, 112113 (2012).

[17] C. J. Cochrane, P. M. Lenahan, and A. J. Lelis, Journal of Applied Physics **105**, 064502 (2009).

[18] B. R. Tuttle, T. Aichinger, P. M. Lenahan, and S. T. Pantelides, Journal of Applied Physics **114**, 113712 (2013).

[19] D. J. Lepine, Physical Review B **6**, 436 (1972).

[20] M. A. Jupina and P. M. Lenahan, IEEE Transactions on Nuclear Science **36**, 1800 (1989).

[21] W. Shockley and W. T. Read, Physical Review **87**, 835 (1952).

[22] R. N. Hall, Physical Review **87**, 387 (1952).

[23] S. M. Sze and K. K. Ng, *Physics of Semiconductor Devices*, 3rd ed. (John Wiley & Sons, 2007).

[24] D. Kaplan, I. Solomon, and N. F. Mott, Le Journal de Physique - Lettres **39**, 51 (1978).

[25] J. A. Weil, J. R. Bolton, and J. E. Wertz, *Electron Paramagnetic Resonance - Elementary Theory and Practical Applications* (Wiley Interscience, 1994).

[26] C. J. Pickard and F. Mauri, Physical Review Letters **88**, 086403 (2002).

[27] J. Vandevondele, M. Krack, F. Mohamed, M. Parrinello, T. Chassaing, and J. Hutter, Computer Physics Communications **167**, 103 (2005).

[28] J. P. Perdew, K. Burke, and M. Ernzerhof, Physical Review Letters **77**, 3865 (1996).

[29] K. Hummer, J. Harl, and G. Kresse, Physical Review B - Condensed Matter and Materials Physics **80**, 115205 (2009).

[30] J. VandeVondele and J. Hutter, Journal of Chemical Physics **127**, 114105 (2007).

[31] T. Hornos, A. Gali, and B. G. Svensson, Materials Science Forum **679-680**, 261 (2011).

[32] F. Jensen, Journal of Chemical Theory and Computation **2**, 1360 (2006).

[33] S. B. Zhang and J. E. Northrup, Physical Review Letters **67**, 2339 (1991).

[34] L. Torpo, M. Marlo, T. E. M. Staab, and R. M. Nieminen, Journal of Physics: Condensed Matter **13**, 6203 (2001).

[35] S. Lany and A. Zunger, Modelling and Simulation in Materials Science and Engineering **17**, 084002 (2009).

[36] S. T. Murphy and N. D. M. Hine, Phys. Rev. B **87**, 094111 (2013).

[37] M. Bockstedte, M. Heid, and O. Pankratov, Physical Review B **67**, 3 (2003).

[38] M. Bockstedte, A. Mattausch, and O. Pankratov, Materials Science Forum **457-460**, 715 (2004).

[39] M. Bockstedte, A. Mattausch, and O. Pankratov, Physical Review B - Condensed Matter and Materials Physics **69**, 1 (2004).

[40] M. Bockstedte, A. Gali, A. Mattausch, O. Pankratov, and J. W. Steeds, Physica Status Solidi B **245**, 1281 (2008).

[41] G. Pensl, F. Ciobanu, T. Frank, D. Kirmse, M. Krieger, S. Reshanov, F. Schmid, M. Weidner, T. Ohshima, H. Itoh, and W. J. Choyke, Microelectronic Engineering **83**, 146 (2006).

[42] J. R. Weber, W. F. Koehl, J. B. Varley, A. Janotti, B. B. Buckley, C. G. Van De Walle, and D. D. Awschalom, Journal of Applied Physics **109**, 102417 (2011).

[43] L. Gordon, A. Janotti, and C. G. Van de Walle, Physical Review B **92**, 045208 (2015).

[44] A. Gali, A. Gällström, N. T. Son, and E. Janzén, Materials Science Forum **645-648**, 395 (2010).

[45] A. Gali, Physica Status Solidi B **248**, 1337 (2011).

[46] A. Gali, Journal of Materials Research **27**, 897 (2012).

[47] V. A. Soltamov, A. A. Soltamova, and P. G. Baranov, Phyiscal Review Letters **108**, 226402 (2012).

[48] W. F. Koehl, B. B. Buckley, F. J. Heremans, G. Calusine, and D. D. Awschalom, Nature **479**, 84 (2011).

[49] M. Widmann, S. Y. Lee, T. Rendler, N. T. Son, H. Fedder, S. Paik, L. P. Yang, N. Zhao, S. Yang, I. Booker, A. Denisenko, M. Jamali, S. A. Momenzadeh, I. Gerhardt, T. Ohshima, A. Gali, E. Janzén, and J. Wrachtrup, Nature Materials **14**, 164 (2015).

[50] K. Szász, V. Ivády, I. A. Abrikosov, E. Janzén, M. Bockstedte, and A. Gali, Physical Review B **91**, 121201 (2015).

[51] See supplemental material at [URL] for a detailed tables of the variation of HF interaction between the various defect symmetry arrangements.

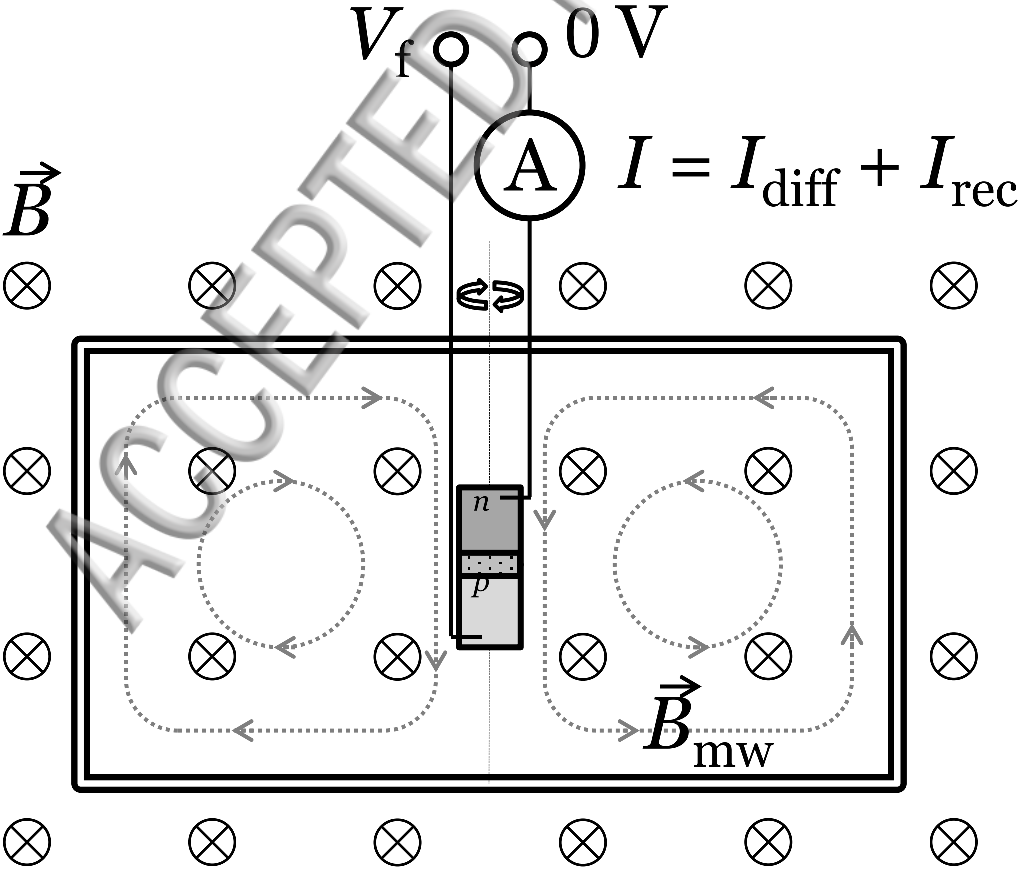
V_f
0 V
A
$I = I_{\text{diff}} + I_{\text{rec}}$
$\vec{B}$
n
p
$\vec{B}_{\text{mw}}$

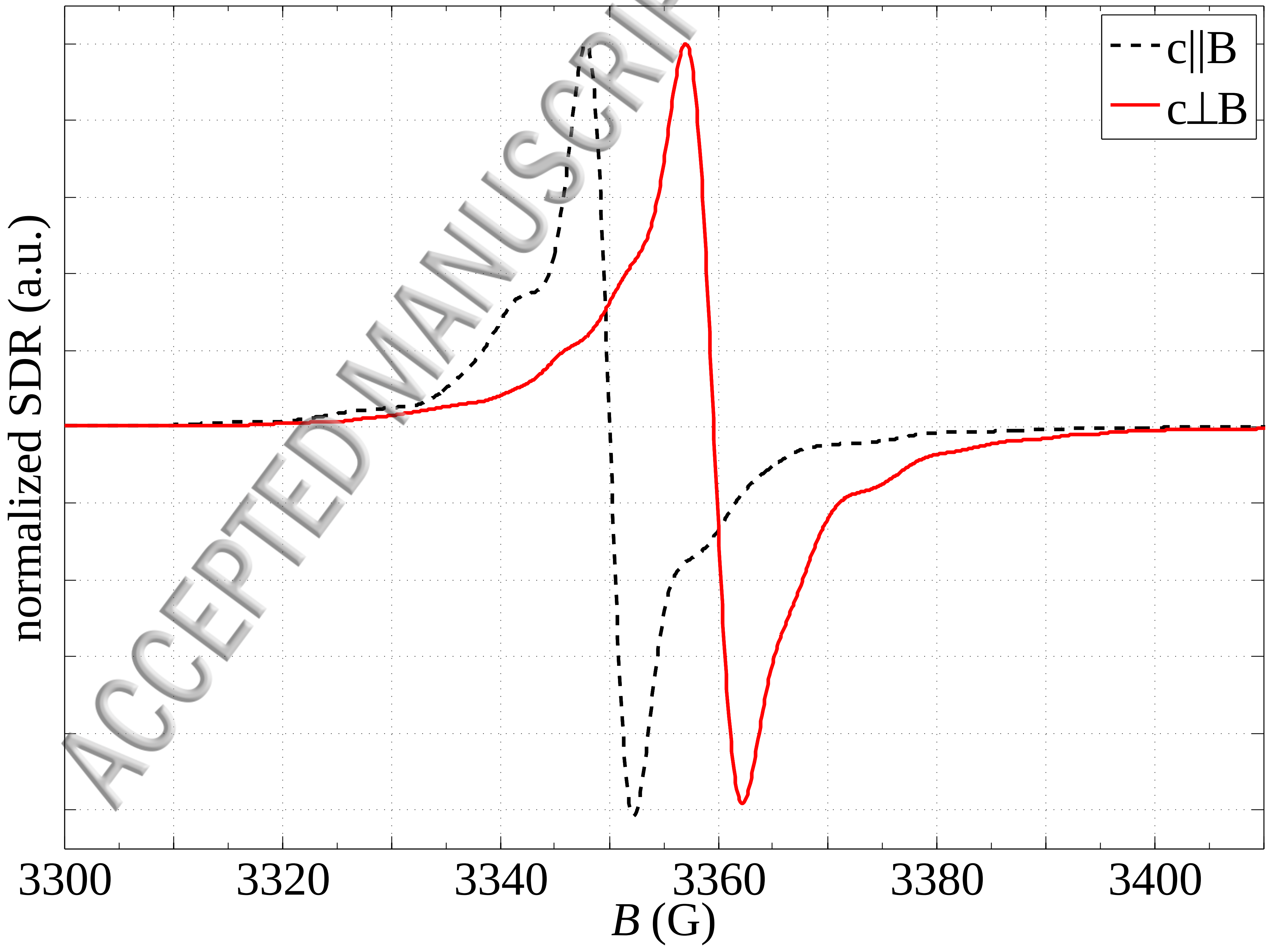
c||B
c⊥B
normalized SDR (a.u.)
3300
3320
3340
3360
3380
3400
B (G)

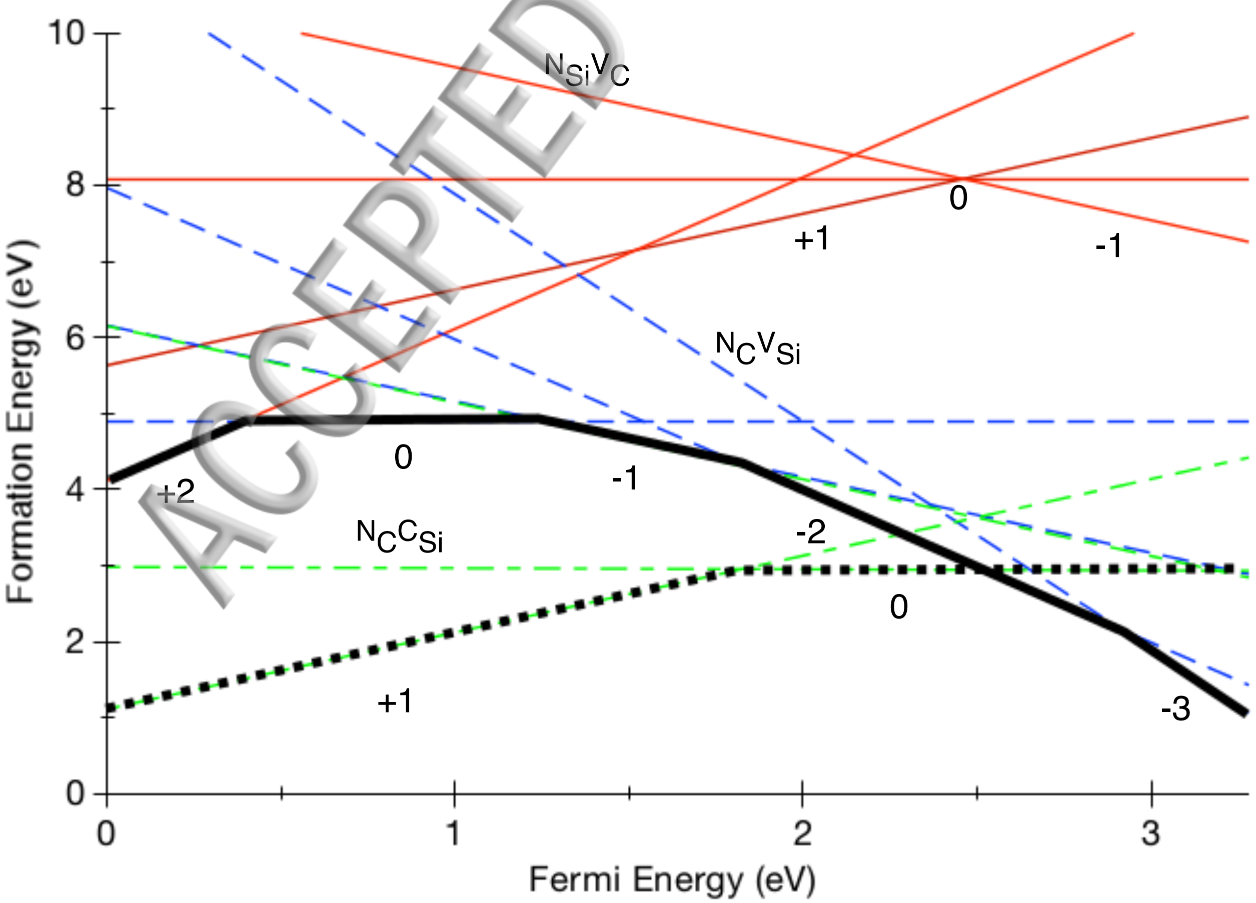

$N_{Si}V_C$
0
+1
-1
N_CV_{Si}
0
+2
-1
-2
-3
N_CC_{Si}
0
+1
Formation Energy (eV)
Fermi Energy (eV)
0
2
4
6
8
10
0
1
2
3

ACCEPTED

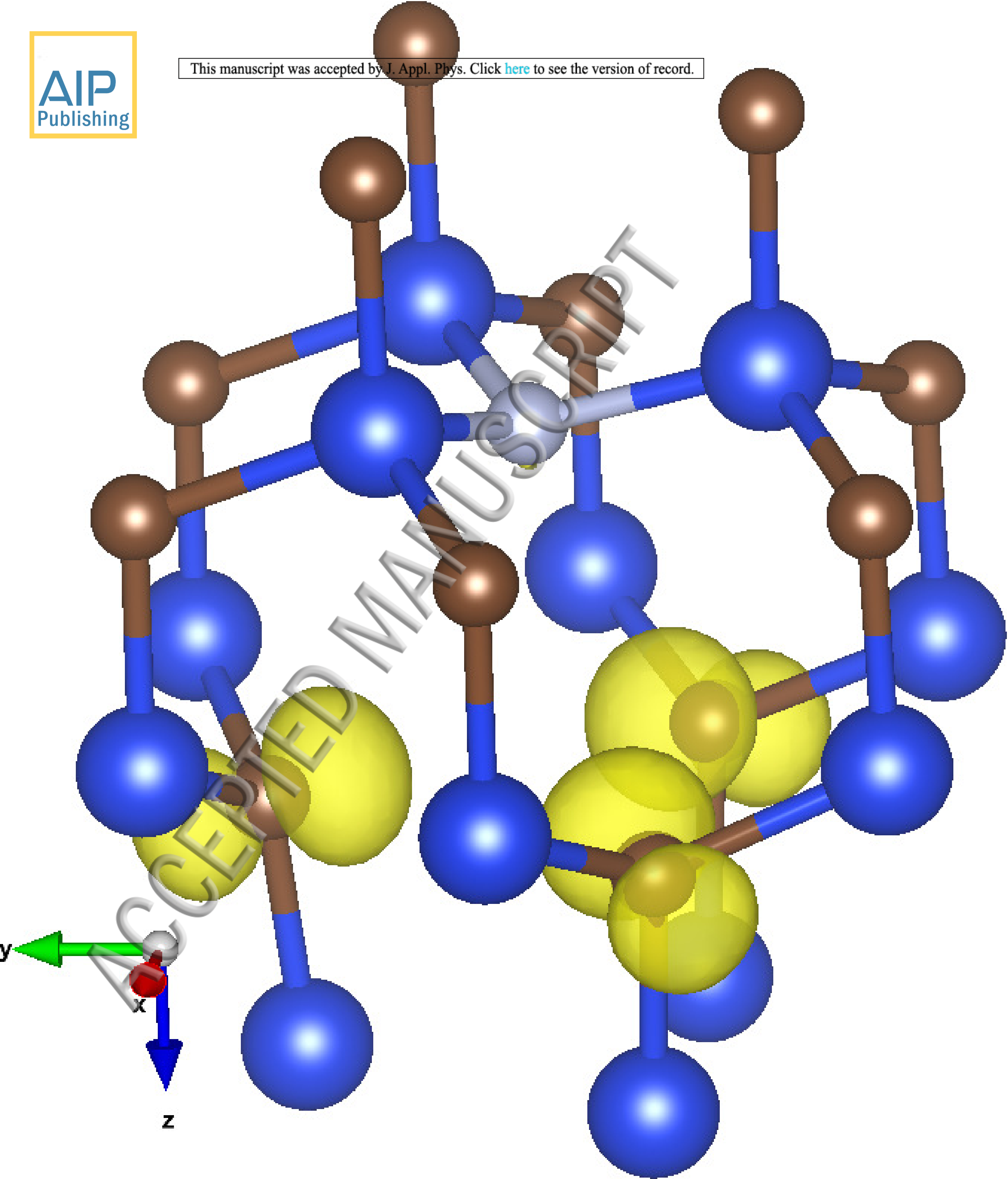
y
x
z

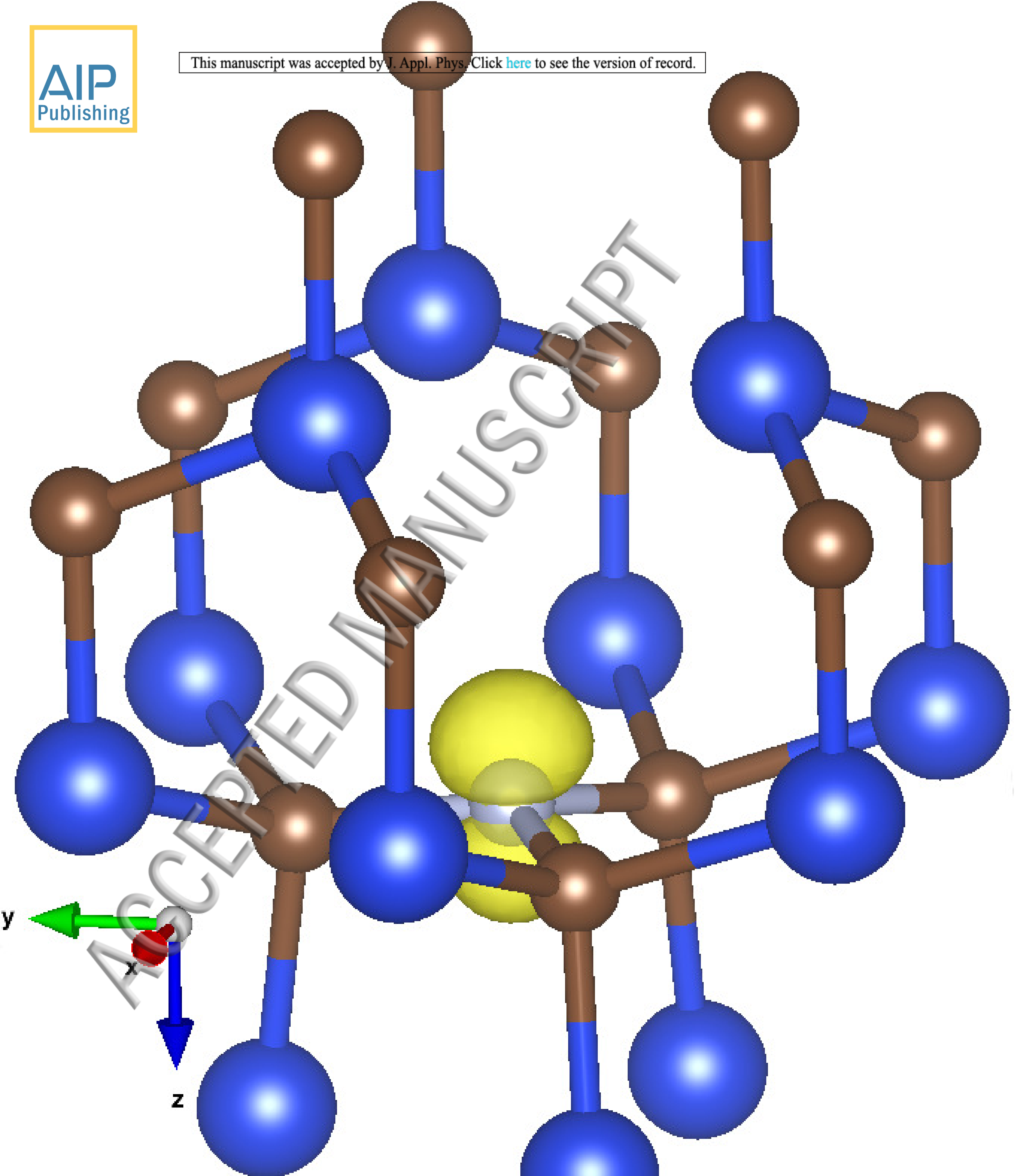
y
x
z

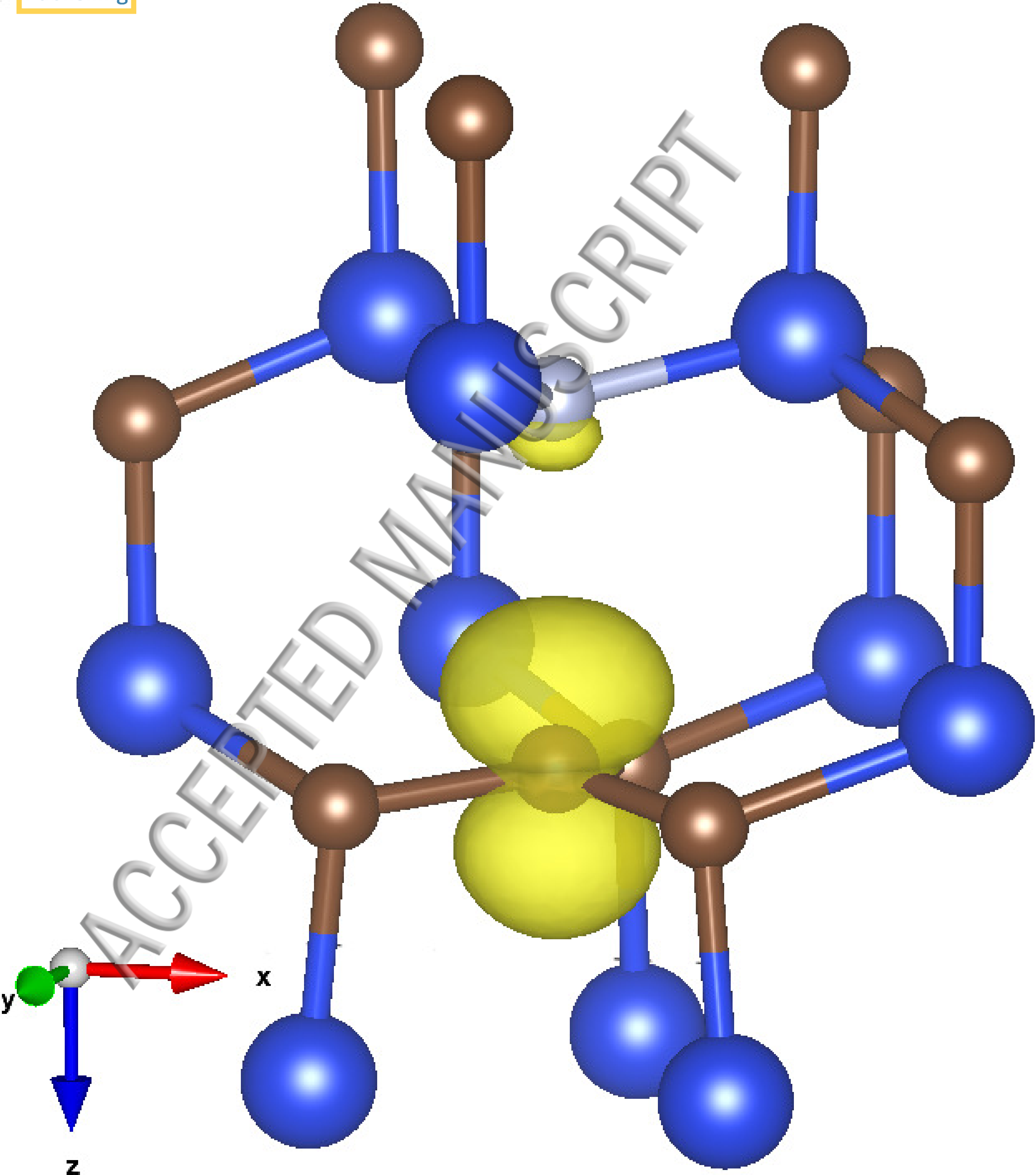
x
y
z

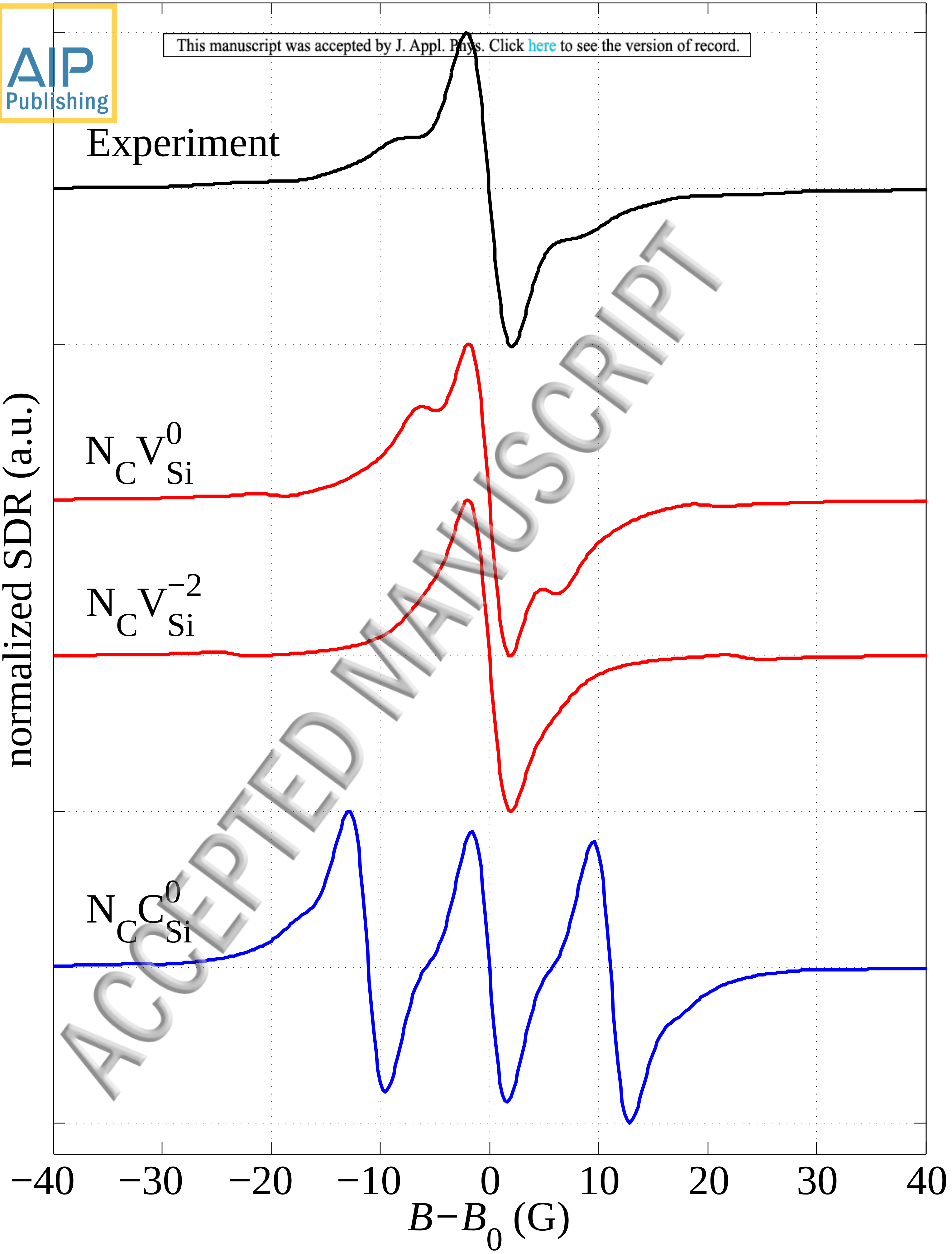
Experiment
$N_CV_{Si}^0$
$N_CV_{Si}^{-2}$
$N_CC_{Si}^0$
normalized SDR (a.u.)
−40
−30
−20
−10
0
10
20
30
40
$B-B_0$ (G)

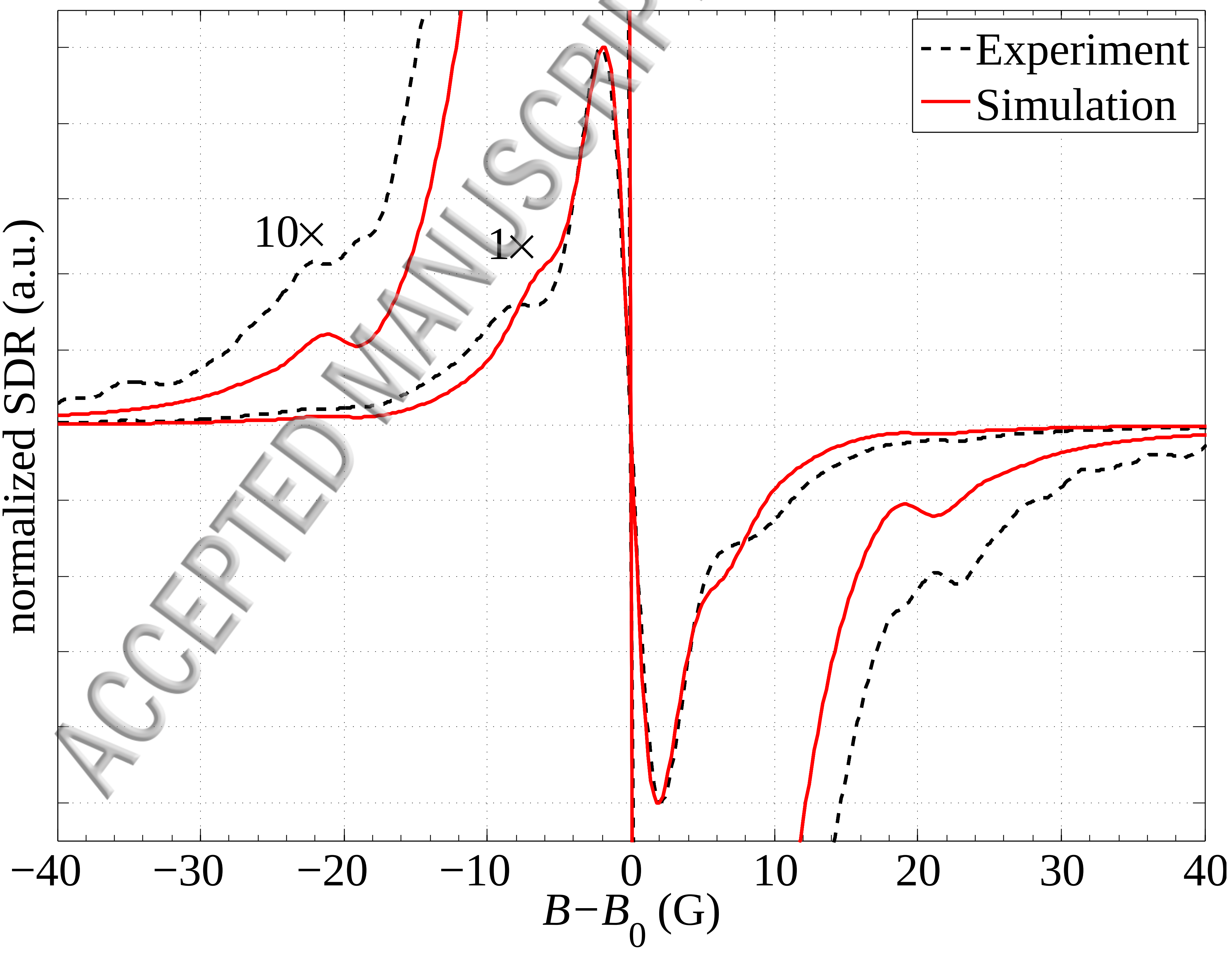
Experiment
Simulation
10×
1×
normalized SDR (a.u.)
−40
−30
−20
−10
0
10
20
30
40
$B-B_0$ (G)

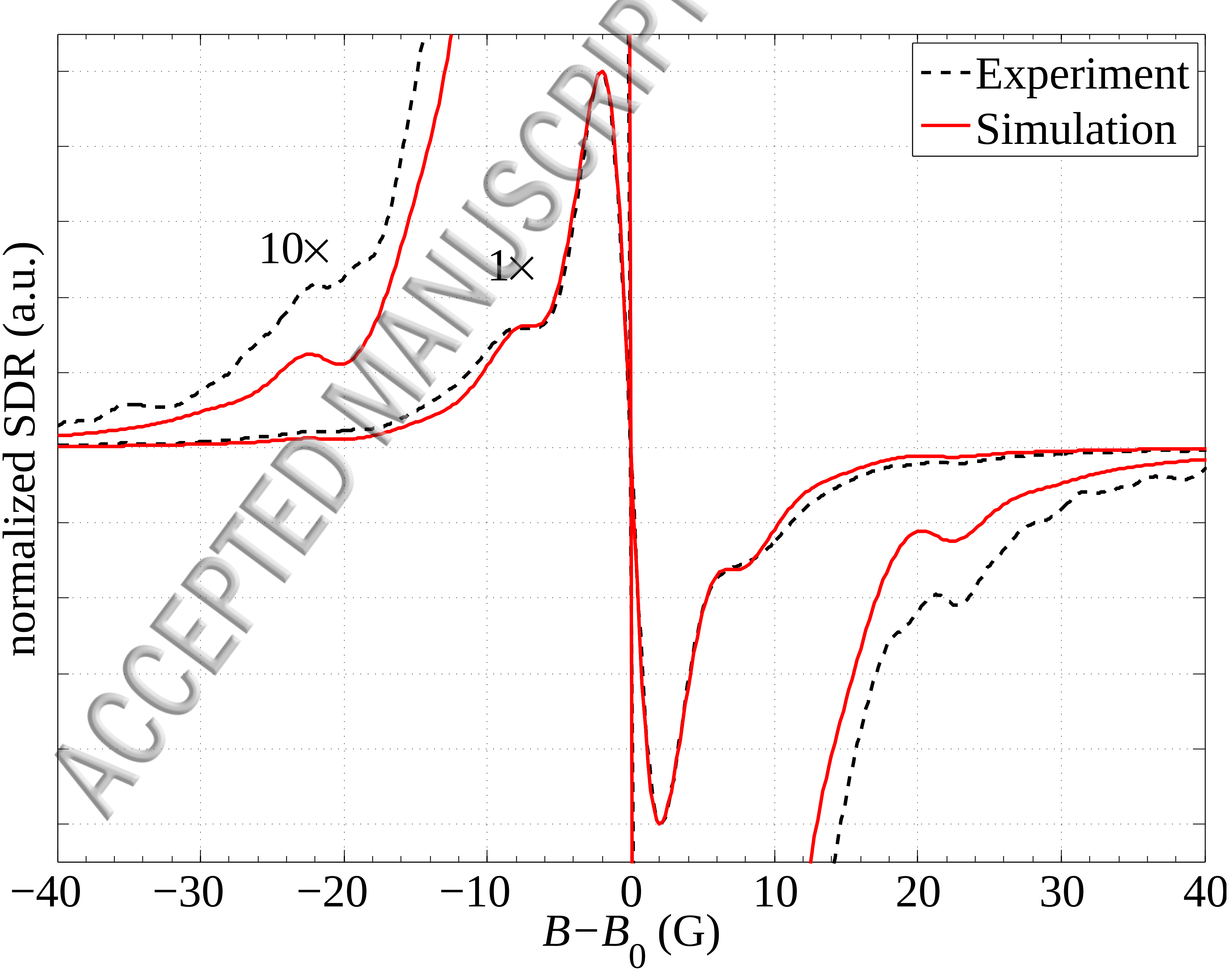

Experiment
Simulation
10×
1×
normalized SDR (a.u.)
−40
−30
−20
−10
0
10
20
30
40
$B-B_0$ (G)